applied sciences

MDPI

Article

Optical System for the Transit Spectral Observation of Exoplanet-Atmosphere Characteristics

Fang Wang [1,2], Xuewu Fan [1,2,*], Hu Wang [1,2], Yue Pan [1,2], Yang Shen [1], Xiaoyun Lu [1,2], Xingqian Du [1,2] and Shangmin Lin [1,2]

[1] Xi'an Institute of Optics and Precision Mechanics of CAS, Xi'an 710119, China; wangfang16@mails.ucas.ac.cn (F.W.); wanghu@opt.ac.cn (H.W.); panyue@opt.cn (Y.P.); shenyang@opt.ac.cn (Y.S.); luxiaoyun15@mails.ucas.ac.cn (X.L.); duxingqian@163.com (X.D.); lsm175@163.com (S.L.)

[2] University of Chinese Academy of Sciences, Beijing 100049, China

* Correspondence: fanxuewu@opt.ac.cn

Abstract: Optical instrumentation with reliable performance is essential for the research of exoplanet atmosphere characteristics. However, due to long distances and weak signals, exoplanets are difficult to be imaged by traditional optical systems. To this end, a novel optical system based on transit spectroscopy is proposed in this paper. On the basis of the principle of the transit-spectroscopy method and the astronomical parameters of observed targets, the optional parameter ranges of a dedicated optical system are analyzed. The transit signal-to-noise ratio (SNR) is introduced for the determination of telescope aperture and throughput. Furthermore, an example of the optical system with a space telescope and spectrometer is proposed according to the above optical index, which is proven to meet the performance requirements. The optical system is required to cover the wavelength of 0.5–8 μm and the field of view (FOV) of 27.9″ within the diffraction limit. The collecting aperture should be greater than 2 m, and spectral resolutions of two spectrometer channels should approximately be 100 (2–4 μm) and 30 (4–8 μm). The point-spread function (PSF) of each channel at the minimal wavelength should cover 2 pixels. The telescope and dichroic system provide diffraction-limited input beams with the required aperture, FOV, and wavelength for the spectrometer slits. The simulation results of the optical system show that the spectral resolutions of the dual-channel spectrometer were 111–200 and 43–94. The image points of the spectrometer in each wavelength were smaller than the Airy spot within the slit FOV, and the full width at half-maximum (FWHM) of PSF at λ_{min} provided 2 pixels of 18 μm sampling. The feasibility of the demonstrated optical parameters is proven by the design.

Keywords: exoplanet atmosphere; transit; optical system; spectrometer; index demonstration; optical design

Citation: Wang, F.; Fan, X.; Wang, H.; Pan, Y.; Shen, Y.; Lu, X.; Du, X.; Lin, S. Optical System for the Transit Spectral Observation of Exoplanet-Atmosphere Characteristics. *Appl. Sci.* **2021**, *11*, 5508. https://doi.org/10.3390/app11125508

Academic Editors: Klaus Michael Spohr and Chien-Hung Liu

Received: 30 March 2021
Accepted: 11 June 2021
Published: 14 June 2021

1. Introduction

With the increasing number of exoplanet discoveries, scientific issues such as verifying the habitability of exoplanets [1], and discussing the relationship between the properties of stars and planetary parameters [2] have become an astronomical research focus that requires the indepth exploration and characterization of exoplanets' internal properties, such as the nature of their atmosphere [3]. However, the faint signals of exoplanets are easily submerged by the huge signals of nearby host stars, which makes it difficult to detect the spectrum of atmosphere characteristics. Optical remote-sensing technology based on transit spectroscopy is the main method to study the properties of a large population of exoplanets. An optical-detection instrument that achieves excellent performance is essential to optimize the results of the transit spectrum.

Many countries carry out optical-instrument projects for observing the spectrum of exoplanets [4]. The James Webb Space Telescope (JWST), developed by the cooperation of multiple organizations, is combined with several scientific payloads to achieve wide-band spectral detection [5]. The Hubble Space Telescope (HST) is extensively used for detecting the atmospheric species of numerous exoplanets, of which the observation using spatial scanning mode is performed for exoplanet transit-spectroscopy studies [6]. Despite the great significance to astronomical studies, these telescopes are general multipurpose facilities having a series of scientific goals as opposed to solely the observation of exoplanets, without simple optical designs and simultaneous wide-band observations. A dedicated survey mission with carefully designed payloads and a stable satellite platform for transit spectroscopy is necessary to study exoplanet-atmosphere characteristics.

According to the characteristics of a transit-spectrum signal, the optional parameter ranges of the corresponding optical system were derived in this paper. The influences of the signal-to-noise ratio (SNR) and number of transits were particularly considered when setting the aperture size and throughput. Furthermore, to overcome the shortcomings mentioned above, an optical system for the transit spectral observation of the atmosphere of exoplanets is presented. The system consists of a space-based telescope with a large collecting area and high optical efficiency, and an infrared spectrometer capable of dual-channel wide-band spectrophotometric detection. The imaging performance of the optical system was simulated in ZEMAX software.

The contributions of this paper are summarized as follows: (1) in order to study the atmosphere characteristics of exoplanets, related optical instrument indices were systematically derived; (2) transit SNR is introduced to the determination of telescope aperture and throughput; and (3) to verify the feasibility of the optical indices, a novel optical system was designed.

2. Astronomical Parameters

2.1. Transit-Spectroscopy Method

Transit spectroscopy is a widely applied method for spectral detection to obtain the atmospheric environmental characteristics of exoplanets. It has relatively low contrast demand (10–100 ppm) and an adequate number of available samples, which is conducive to studying warm and hot exoplanets with a short period and nearby orbit [7]. Among five complementary methods for transiting planets [8], primary and secondary transits (eclipse) have great significance for studying the atmospheric composition of exoplanets; they were selected as the detection methods in this paper.

The detection principle of the primary transit-spectroscopy method is shown in Figure 1. When a planet passes in front of its host star, the latter is partially blocked, and its luminous flux is reduced by a few percentage points. The reduction in percentage corresponds to the ratio of the projected area of the planet and star (transit depth), and the radius of planet can be inferred from the flux measurement. When starlight transmits through the atmosphere on a planetary terminator, additional specific wavelength absorption occurs corresponding to the signatures of molecular species in the atmosphere, which varies the transit depth at different wavelengths. Light curves at different wavelengths are marked in red, green, and blue in Figure 1a. The light curve at each wavelength has a characteristic transit depth in the periods of duration (T_{14}), ingress (T_1–T_2) and egress (T_3–T_4) [9]. Secondary transit (eclipse) spectroscopy has a similar principle. When a planet orbits behind the host star, the planet is occulted, resulting in a drop in flux. Since the planet flux including the contribution of planetary atmosphere is removed, an eclipse light curve is produced [10]. Thus, information of planetary-atmosphere composition can be inferred from the spectral characteristics.

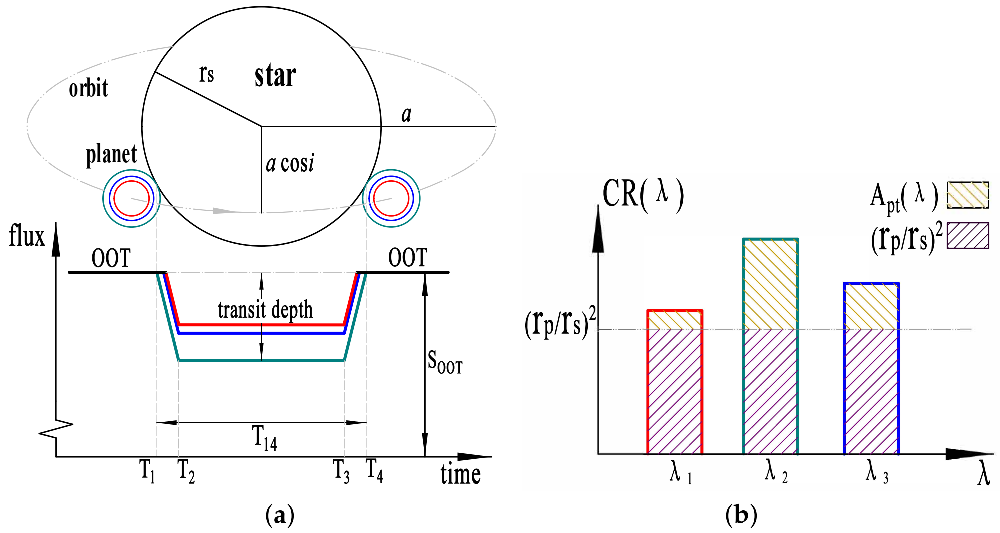

Figure 1. (**a**) Primary transit spectroscopy with light curves at different wavelengths. T_2 and T_3 indicate the time when the planetary projection completely enters and just exits the star. (**b**) Chart of contrast-ratio composition. Contrast ratio is composed of constant planetary component $(r_p/r_s)^2$, as indicated by the horizontal line, and wavelength-dependent atmospheric contribution $A_{pt}(\lambda)$. Red, blue, and green lines represent observation results at different wavelengths.

2.2. Transit-Spectroscopy Parameters

In order to obtain the infrared transmission spectrum from a planetary terminator atmosphere during primary transit and the blocked atmospheric spectrum in secondary eclipse, relevant spectral-signal parameters need to be calculated.

Transit spectroscopy relies on the measurements of a multiwavelength high-precision light curve when the exoplanet passes by the host star. Each light curve has different characteristic transit depths during transit, measured by the contrast ratio (CR) between the transit depth during the primary transit and the extrasolar system flux while out of transit (OOT) [11]. The CR is defined as

$$CR(\lambda) = \frac{S_{OOT}(\lambda) - S_{IT}(\lambda)}{S_{OOT}(\lambda)} = \frac{S_p(\lambda) + S_A(\lambda)}{S_{OOT}(\lambda)}, \tag{1}$$

where $S_{IT}(\lambda)$ and $S_{OOT}(\lambda)$ are spectral signals measured in and out of transit, respectively. $S_{OOT}(\lambda) - S_{IT}(\lambda)$ is the reduced part of a star signal during transit that has two components, namely, the star signal blocked by the planet alone, $S_p(\lambda)$, and the star signal absorbed by the planetary atmosphere, $S_A(\lambda)$. When a simplified system model with absence of limb darkening is adopted, the ratio between the signal blocked by the planet and the OOT star signal is a constant at any wavelength, corresponding to the projected area ratio of the planet and star, i.e., $S_p(\lambda)/S_{OOT}(\lambda) = (r_p/r_s)^2$, where r_p and r_s are the radii of the planet and star, respectively. $S_A(\lambda)/S_{OOT}(\lambda)$ can be regarded as additional wavelength-dependent contribution [12] coming from the atmosphere, $A_{pt}(\lambda)$, as shown in Figure 1b. The CR spectrum with atmospheric absorption [13] can be expressed as

$$CR(\lambda) = (r_p/r_s)^2 + A_{pt}(\lambda). \tag{2}$$

Atmospheric contribution at any wavelength $A_{pt}(\lambda)$ in Equation (2) can be established as follows.

$$A_{pt}(\lambda) \approx n_H(\lambda) \frac{2r_p}{r_s^2} \frac{kT_p}{g\mu}, \tag{3}$$

where k is the Boltzman constant, T_p is the mean planetary atmospheric temperature, μ is the mean molecular mass, g is surface gravity, and $n_H(\lambda)$ is the scale factor, which depends on feature intensity, varying with opacity [14].

The calculation results of Equation (3) in a variety of planetary systems show that a transit signal is more obvious around smaller stars, and the frequency of transits also increases, which allows for utilizing more revisits to improve the SNR. Therefore, the signal of a planet is higher around an M dwarf, which is called "M-dwarf advantage" [15]. This should be taken into account when selecting planetary candidates as observation targets.

The SNR of atmospheric contribution is given by the ratio of A_{pt} to noise. The noise and SNR [16] on $A_{pt}(\lambda)$ of single transit in any spectral bin can be, respectively, approximated by

$$\sigma_{A_{pt}}(\lambda) = \frac{\sqrt{2t}}{\sqrt{T_{14}}} \frac{\sigma_{OOT}(\lambda)}{S_{OOT}(\lambda)} \tag{4}$$

and

$$SNR_{A_{pt}}(\lambda) = \frac{A_{pt}(\lambda)}{\sigma_{A_{pt}}(\lambda)} = \frac{A_{pt}(\lambda)\sqrt{T_{14}}}{\sqrt{2t}} SNR_{OOT}(\lambda), \tag{5}$$

where $S_{OOT}(\lambda)$ represents the total observed signal of single exposure at the wavelength of λ in the OOT period, $\sigma_{OOT}(\lambda)$ is the noise on $S_{OOT}(\lambda)$, $SNR_{OOT}(\lambda)$ is the corresponding signal-to-noise ratio, and t is the single exposure time. T_{14} is the transit time in Figure 1a, defined as the planet traveling duration from ingress to egress

$$T_{14} = \frac{Pr_s}{\pi a} \sqrt{\left(1 + \frac{r_p}{r_s}\right)^2 - \left(\frac{a \cos i}{r_s}\right)^2}, \tag{6}$$

where i, a, and P are the planetary orbital inclination, semimajor axis, and period, respectively [17].

The value of $SNR_{A_{pt}}$ is generally too small to meet the requirements, so it is necessary to combine multiple transit observations to realize targets. In order to achieve a goal SNR, the number of transits is given by

$$N_{transit} = \left(\frac{SNR_{goal}}{SNR_{A_{pt}}}\right)^2. \tag{7}$$

These are also applied to parameter estimation in a secondary eclipse, of which the substituted atmospheric contribution and SNR are expressed as $A_{se}(\lambda)$ and $SNR_{A_{se}}(\lambda)$,

$$A_{se}(\lambda) = \frac{B_\lambda(T_p)}{B_\lambda(T_s)} \left(\frac{r_p}{r_s}\right)^2 + \rho\left(\frac{r_p}{a}\right)^2 \tag{8}$$

and

$$SNR_{A_{se}}(\lambda) = \frac{A_{se}(\lambda)}{\sqrt{2}} SNR_{OOT}(\lambda), \tag{9}$$

where $B_\lambda(T_p)$ and $B_\lambda(T_s)$ are the Planck function for the planet and star, respectively, and ρ is the geometric albedo.

3. Optical Indices

In order to detect the atmospheric characteristics of exoplanets, a specifically designed optical instrument with stable payloads is valuable. Before designing an optical system, it is necessary to determine the optical indices of the telescope and spectrometers.

On the basis of the influence of telluric contamination on wavelength coverage and the duration of transit observations, a space- rather than ground-based telescope was adopted. Considering the maximization of sky field of view (FOV) and thermal stability, a space telescope operating in the L2 Lissajous orbit was the optimal solution for the mission [18]. Optical indices are discussed in this condition.

3.1. Wavelength Coverage and F Number

In order to more effectively detect a target signal, wavelength coverage with strong radiation for target planetary systems and weak radiation for background should be considered. The black-body radiations of observed objects appear more intensely in the range of 0.5–8 µm [19]. The zodiacal emission emerges as a peak in 0.35–0.55 µm, and significantly decreases in the near-infrared band above 2 µm, though it slightly increases at a larger wavelength under the impact of a thermal-emission component, as shown in Figure 2 [20].

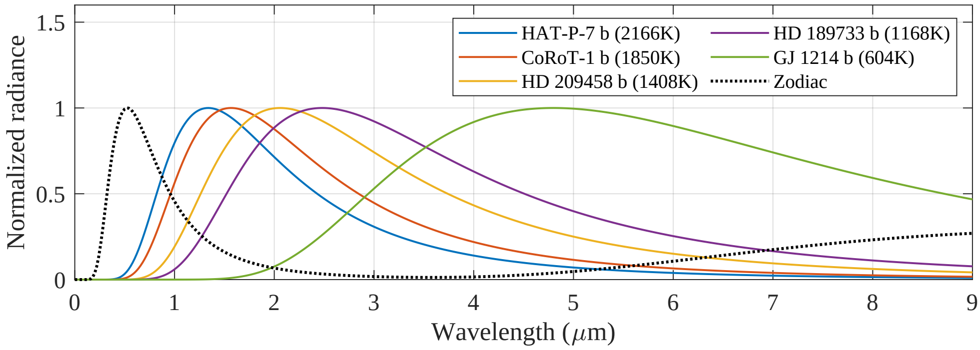

Figure 2. Normalized radiance of several exoplanet candidates and zodiacal background.

Furthermore, the main atmospheric species, including H_2O, CO_2, and CH_4, have obvious absorption characteristics at 2–8 µm, while the molecular curve at shorter wavelength is relatively smooth [21]. Additionally, broadband coverage is a beneficial for breaking the degeneracy of the spectra of different species, which ensures the retrieval of molecular abundance [22]. Consequently, wavelength coverage of 2–8 µm for the spectrometer and 0.5–2 µm for the pointing system were selected.

Limited by the optical materials and detector indicators, the spectral coverage of 2–8 µm was too wide to meet the detection requirements in a single channel. Considering that a wavelength around 4 µm is not the absorption of a certain atmosphere, the spectrometer was split into two wavelength channels with 2–4 µm and 4–8 µm, named CH1 and CH2, respectively. Because the full width at half-maximum (FWHM) of point-spread function (PSF) is required to cover at least two pixels at each channel, the relationship between F number and pixel size l_{pix} is shown as Equation (10). The F numbers of two channels were set to $F_{CH1} = 14.754$ and $F_{CH2} = 7.337$ in l_{pix} = 18 µm.

$$1.22\lambda_{\min}F = 2l_{pix} \tag{10}$$

3.2. Spectral Resolution and SNR

The lowest limits of spectral resolution (R) and SNR must satisfy the accuracy requirements of atmospheric-retrieval results, that is, the ability to separate two adjacent J components of the molecular band, which is considered to be the recognition of spectral features [23]. However, a higher resolution leads to larger spectral-line dispersion. Larger dispersion results in the spectral energy of the required band being dispersed into more pixels, which leads to an increase in the ratio of detector noise to total noise.

The impact of SNR and spectral resolution on the retrievability of model parameters (planetary temperature, molecular abundances, and cloud parameters) from transit spectra was investigated by utilizing retrieval code TauREx [24]. The error of spectral retrieval was simulated as a function of the spectral resolution and SNR, and results were obtained in the case of hot Jupiter and warm Neptune [25]. Results indicate that a spectrum with an SNR of approximately 10 (denoted as $\sim$10) and R $\sim$ 100 could retrieve the chemical molecule well. There were noticeable improvements in temperature retrieval from SNR 5–10 and R 30–100. SNR $\sim$ 20 and R $\sim$ 200 had very accurate results, but there was no obvious improvement with a higher SNR and R.

Combined with the present technical level, the goal SNR was set to be $SNR_{goal} \sim 7$, $R \sim 100$ (2–4 μm), $R \sim 30$ (4–8 μm). Dim targets need to be revisited many times to achieve the above requirements. For a planetary system with an obvious signal, the SNR can be up to 10–20, which is conducive to deeper measurements.

3.3. Telescope Aperture and Overall Throughput

The telescope aperture and overall throughput of optical instruments affect some of the noise components and the stellar signal, which changes the single-transit observation SNR and the required number of revisits; thus, the selection of aperture and throughput should be interconnected with the $N_{transit}$ and the SNR_{goal} mentioned in Section 2.2.

3.3.1. Stellar Signal

Spectral radiant emittance of target stars M is a function of observed wavelength λ, star magnitude m, and absolute temperature T:

$$M(m,\lambda,T) = K_0(m,T)B(\lambda,T) = K_0(m,T)\frac{2hc^2}{\lambda^5(\exp(hc/kT\lambda)-1)}, \tag{11}$$

where $B(\lambda,T)$ is the Planck black-body radiation formula, h is the Planck constant, c is the speed of light in vacuum, and k is the Boltzmann constant. $K_0(m,T)$ is the calibration parameter, which is established corresponding to the observed star by defining the magnitude zero with A_0 star. When the target star is given with a fixed magnitude and temperature, $M(\lambda)$ is a function of wavelength [26].

The relationship between emittance from the star surface and spectral irradiance in the primary telescope mirror is denoted as $E_{tel}(\lambda)$, while the distance from optical system to star is D:

$$E_{tel}(\lambda) = M(\lambda)\left(\frac{r_s}{D}\right)^2. \tag{12}$$

The light energy received by the telescope has certain attenuation after passing through optical elements. The overall throughput of the optical system, $\tau(\lambda)$, is the product of each optical element, which should consider the influence of lens transmittance, mirror reflectivity, and lens material absorption, expressed as

$$\tau(\lambda) = \prod_i t_i(\lambda)\prod_j p_j(\lambda)\prod_k(1-\alpha_k(\lambda))^{d_k}, \tag{13}$$

where $t_i(\lambda)/p_j(\lambda)$ is the transmittance or reflectivity of the i-th/j-th transmission or reflection surface, and α_k and d_k are the material absorption coefficient and element thickness of the k-th transmission element, respectively.

The photoelectron count caused by the stellar signal in each spectral bin per exposure during the OOT period can be approximately calculated by

$$S_{OOT}(\lambda) = A_{tel}E_{tel}(\lambda)\tau(\lambda)tQE(\lambda)\delta\lambda\left(\frac{hc}{\lambda}\right)^{-1}, \tag{14}$$

where A_{tel} is the collection area of the primary mirror, $QE(\lambda)$ is the quantum efficiency of the detector pixels for each wavelength, and $\delta\lambda$ is the span of each spectral resolution element [15].

3.3.2. Total Noise

Noise is expressed here as the standard deviation of noise in spectral bins. Although the noise of atmospheric signals cannot be obtained in actual measurements, it has a proportional relationship with OOT noise according to Equation (4), so it is necessary to estimate atmospheric signal noise and evaluate the performance of the instrument by measuring OOT noise.

The noise sources to be included in the calculation of $\sigma_{OOT}(\lambda)$ are [27]: (1) photon noise from the target source, (2) zodiacal background noise, (3) thermal-radiation noise from the instrument, (4) dark current noise, and (5) readout noise. Photon noise and background noise belong to uncorrelated astrophysical noise sources that produce shot noise obeying Poisson distribution; standard deviation is the square root of the signal. Therefore, the noise component (noise/signal) decreases with stronger signals and longer integration time.

Zodiacal background radiation is related to the ecliptic latitude location of the target star. On the basis of the photometric model [28], zodiacal spectral radiance $L_{zodi}(\lambda)$ in W/m^2/µm/sr was established as

$$L_{zodi}(\lambda) = 3.5 \times 10^{-14} B_\lambda(5500K) + 3.58 \times 10^{-8} B_\lambda(270K), \tag{15}$$

where $B_\lambda(270K)$ is the Planck function for the thermal-emission component of the interplanetary dust cloud, and $B_\lambda(5500K)$ for the scattered-light component. Zodiacal light is transmitted through the instrument and converges on the focal plane, producing photoelectrons in each spectral bin per exposure as

$$S_{zodi}(\lambda) = L_{zodi}(\lambda)\tau(\lambda)tQE(\lambda)A_{pix}\Omega_{pix}\delta\lambda\frac{\lambda}{hc} * C(\lambda), \tag{16}$$

where A_{pix} is the area of a pixel, and Ω_{pix} is the solid angle at the pixel. $*$ denotes a convolutional operation, and $C(\lambda)$ is the boxcar function related to a spectrometer slit image.

Infrared thermal-radiation noise from the instrument is the sum of the thermal emissions of every optical element subsequent transmitted, of which the energy is calculated from each emissivity element $\epsilon(\lambda)$ multiplied by Planck function $B_\lambda(T)$. The spectral radiance of the instrument's thermal-radiation component reaching the detector is

$$L_{emm}(\lambda) = \sum_{i=1}^{N-1}\left(\epsilon_i(\lambda)B_\lambda(T_i)\prod_{k=i+1}^{N}\tau_k(\lambda)\right) + \epsilon_N(\lambda)B_\lambda(T_N), \tag{17}$$

where N is the number of optical elements, and $\epsilon_i(\lambda)$ and T_i are the emissivity and temperature of the i-th element, respectively. Similar to the zodiacal background, thermal-radiation noise from the instrument is measured as

$$S_{emm}(\lambda) = L_{emm}(\lambda)\tau(\lambda)tQE(\lambda)A_{pix}\Omega_{pix}\delta\lambda\frac{\lambda}{hc} * C(\lambda). \tag{18}$$

It was assumed that there was no correlation noise in the simplified model, and the effects of limb darkening and jitter noise were negligible [29]. The theoretical variance of the total noise composed of the above-mentioned sources per exposure is

$$\begin{aligned}\sigma^2_{total}(\lambda) =&\sigma^2_{star}(\lambda) + \sigma^2_{zodi}(\lambda) + \sigma^2_{emm}(\lambda) + \sigma^2_{dc}(\lambda) + \sigma^2_{rn}(\lambda)\\ =&S_{OOT}(\lambda) + S_{zodi}(\lambda) + S_{emm}(\lambda) + N_{pix}(\lambda)I_{dc}t + 2N_{pix}(\lambda)\sigma^2_{rpix},\end{aligned} \tag{19}$$

where $\sigma^2_{star}(\lambda)$ is photon noise from the target source, $\sigma^2_{zodi}(\lambda)$ is zodiacal-background noise, $\sigma^2_{emm}(\lambda)$ is thermal-radiation noise from the instrument, $\sigma^2_{dc}(\lambda)$ is dark-current noise, $\sigma^2_{rn}(\lambda)$ is readout noise of the detector with correlated double sampling, $N_{pix}(\lambda)$ is the number of pixels corresponding to each spectral resolution element, I_{dc} is the single-pixel dark current, and σ^2_{rpix} is the single-pixel readout-noise variance. Total noise distribution expressed as standard deviation is

$$\sigma_{OOT}(\lambda) = \sqrt{\sigma^2_{total}(\lambda)}. \tag{20}$$

3.3.3. Selection of Telescope Aperture and Overall Throughput

According to the $S_{OOT}(\lambda)$ and $\sigma_{OOT}(\lambda)$ deduced above, $SNR_{A_{pt}}(\lambda)$, $SNR_{A_{se}}(\lambda)$ and $N_{transit}$ can be estimated as in Equations (5), (7), and (9). The observation feasibility of the selected astronomical targets is judged by comparing $N_{transit}$ with the maximal number N_{limit} of possible transits during the mission, $N_{limit} = L_{tel}/P$, where P is the orbital period of the planet and L_{tel} is the operation lifetime of the mission.

The ExoSim simulator [30] was used as the test tool to calculate the required transit number achieving the SNR_{goal} under different throughputs τ and telescope apertures D_{tel}, where $D_{tel} = 2\sqrt{A_{tel}/\pi}$. Planetary system GJ 1214 b [31] was assumed as an example of an observation target, of which the parameters are shown in Table 1. GJ 1214 b is considered to have abundant atmospheric molecular species, which makes it an excellent example for detecting the atmospheric characteristics by transit spectroscopy. It is also representative of a warm super-Earth orbiting an M dwarf star, imposing challenges to transit observation. When GJ 1214 b proved to be a feasible sample for the optical system, a large number of planetary targets were detectable. Planetary atmospheric contribution A_{pt}, as shown in Equation (3), adopts further approximation assuming that the full-band starlight is completely absorbed by the atmosphere when $n_H(\lambda) = 5$ [23]. The energy distribution of stellar radiation adopts the Phoenix model [32], and the linear limb darkening coefficient was set to 0.2674 [33]. The emissivity of the optical element was set to 0.03, and operating temperature was 70 K. Detector properties refer to the indices of Teledyne H1RG detector [34] with a single exposure time of 20 s. Systematics could be considered and tested by ExoSim. Uncertainty from systematic noise sources is quantified in ExoSim by capturing complex time-domain effects and performing Monte Carlo simulations to obtain the spectral distribution of transit depths.

The test results are shown in Table 2 with a fixed telescope diameter. SNR_1, adopting the mean value of $SNR_{A_{pt}}$ and $SNR_{A_{se}}$, was calculated as the average of each channel over the wave band in a single transit observation, which varies with the overall throughput of optical system. Under the condition of $SNR_{goal} = 7$, numbers of transits $N_{transit}$ were also calculated and are listed in the table, as well as the average $N_{transit}$ in two channels.

Table 1. Parameters of GJ 1214 b exoplanet system.

Exoplanet system	Super-Earth GJ 1214 b
Star features	M4.5 dwarf, 0.2213 $R_{\odot}$, 0.176 $M_{\odot}$, mag_K = 8.782
Star Phoenix model	T = 3000 K, log g = 5.0, [Fe/H] = 0
Planetary parameters	P = 1.58 d, 6.55 $M_{\oplus}$, 2.84 $R_{\oplus}$, T_p = 604 K, μ = 18 g/mol, T_{14} = 3161 s
$\mathbf{A_{pt}}$	282.78 ppm

Table 2. SNR_1 and $N_{transit}$ values varying with throughput when D_{tel} = 2 m for GJ 1214 b.

τ (D_{tel} = 2 m)	CH1		CH2		Average $N_{transit}$
	SNR_1	$N_{transit}$	SNR_1	$N_{transit}$	
0.3	0.573	149	0.704	99	124
0.4	0.671	109	0.819	73	91
0.5	0.751	87	0.919	58	73
0.6	0.831	71	1.015	48	60
0.7	0.898	61	1.095	41	51
0.8	0.93	53	1.173	36	45
0.9	1.019	47	1.239	32	40

The change in D_{tel} made SNR_1 and $N_{transit}$ different. Using the same method, the relationship between the optical-instrument parameters and the average $N_{transit}$ of two channels is shown in Figure 3. A larger telescope aperture means a larger collection area for the optical system, which leads to an increase in SNR_1 and decrease in $N_{transit}$. In addition, when the aperture and other parameters of instrument are determined, the promotion of overall throughput also contributes to a higher SNR_1 and lower $N_{transit}$.

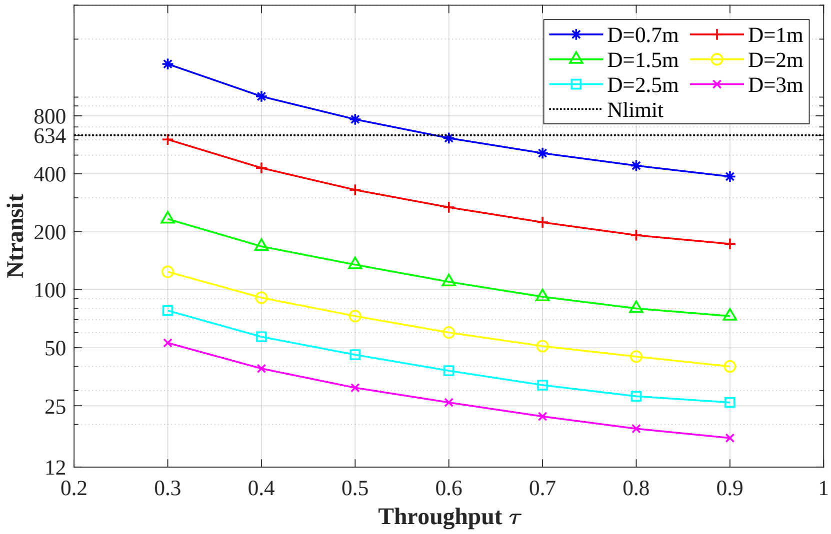

Figure 3. Number of transits to achieve SNR_{goal} under different apertures and throughput for GJ 1214 b.

However, the telescope aperture and overall throughput are limited by the actual capacity for processing and assembling [35]. Considering factors of mirror deformation, detector ability, pupil aberration, and requirements for a lightweight and miniaturized space telescope, it is a great challenge for a very large mirror; therefore, a reasonable aperture size should be selected in combination with SNR requirements. Transit times can be up to $N_{limit} = 634$ for GJ 1214 b within a mission lifetime of 1000 days, but the actual number of revisits is far smaller than this value. Therefore, according to the relationship between transit times and instrument characteristics, aperture and throughput can be set as $D_{tel} \geq 1.5$ m and $\tau \geq 0.4$, respectively.

Parameter settings are based on a challenging case of GJ 1214 b. To verify the feasibility of the parameter settings, simulations for other exoplanets were conducted. As shown in Table 3, A_{pt} and demanded $N_{transit}$ for hotter and larger planets were simulated under the condition of D_{tel} = 2 m, $\tau = 0.5$. Results indicate that the goal SNR could be reached when combined with several transit observations.

Table 3. Atmospheric contribution and number of transits for representative exoplanets under condition of D_{tel} = 2 m, $\tau = 0.5$.

Exoplanets	A_{pt}	$N_{transit}$
hlHD209458b	8.31227×10^{-4}	1
HD189733b	5.16466×10^{-4}	1
WASP-13b	6.21407×10^{-4}	5
WASP-34b	9.91337×10^{-4}	8
HAT-P1b	6.92584×10^{-4}	10
HAT-P26b	1.00658×10^{-3}	10
WASP-12b	7.61745×10^{-4}	13

3.4. Field of View

Different from an imaging spectrometer, an optical system based on the transit-spectroscopy method is a spectrophotometer without the angular-resolution requirement that is utilized to image a single point object at infinity. Under the condition of an ideal image, only the central FOV is needed. However, due to the existence of an Airy spot, an extra FOV around the central FOV should also be accepted to image the target star. Thus, when the FOV of the optical system is calculated, the Airy spot and pointing accuracy of payloads need to be considered [36].

The pointing system, referring to the structure and performance of ARIEL-FGS [37], ensures that the target falls into the FOV by regulating the absolute pointing error (APE). The FOV of the pointing system is expressed in *arcsec* as follows.

$$FOV_{FGS} \geq \frac{2 \times 1.22\lambda_{max}}{D_{tel}} \frac{180 \times 3600}{\pi} + 2APE_c. \tag{21}$$

Similarly, the FOV requirement of spectrometer in the spectral direction is

$$FOV_{IRS} \geq \frac{2 \times 1.22\lambda_{max}}{D_{tel}} \frac{180 \times 3600}{\pi} + 2APE_f. \tag{22}$$

The maximal wavelength for the pointing system is λ_{max} = 2 µm, and for the two channels of the spectrometer is $\lambda_{max(CH1)}$ = 4 µm and $\lambda_{max(CH2)}$ = 8 µm. The APE in coarse- and fine-pointing mode adopt $APE_c = 8''$ and $APE_f = 1''$, respectively. An extended FOV of $\pm 10''$ in the spatial direction of the spectrometer monitors the background using off-source pixels. Assuming that the telescope aperture is fixed as D_{tel} = 2.1 m, the FOV requirements of each optical channel are summarized in Table 4.

The overall instrument FOV should both include the requirements of payloads, and consider the additional FOV generated from the assembly process, such as the misalignment between telescope and payload modules. Therefore, a margin of 12″ must be attached to the half FOV mentioned above. The final field of view of the telescope is shown in Table 4. Figure 4 shows the layouts of the telescope FOV with the ideal alignment and final dimensions with an additional margin.

Table 4. Summary of field of view (FOV) requirements.

Designation	FOV (arcsec)	Comments
CH1	3×20	CH1 requires rectangular FOV with spectral direction of 3″ and spatial direction of 20″.
CH2	3.9×20	CH2 requires rectangular FOV with spectral direction of 3.9″ and spatial direction of 20″.
Pointing system	16.5	Pointing system requires a 16.5″ circular FOV.
Telescope with diffraction limit	27.9	Telescope is diffraction-limited within 27.9″ to ensure well-resolved point-spread function (PSF) at the slit center.
Telescope with pointing acquisition	40.5	Telescope FOV within 41.5″ allows for capturing a star and locating it in the slit center.
Telescope with background	44	Edge of telescope FOV is extended to 44″ to capture slit background, demanding to be unvignetted to ensure that photons enter the slit without obstacles.

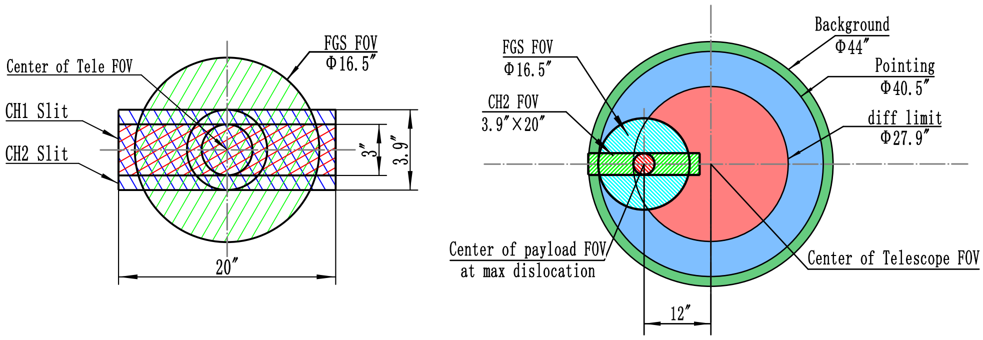

(**a**) (**b**)

Figure 4. (**a**) FOV of pointing system (green) and spectrometers (red CH1, blue CH2) when ideally aligned. (**b**) Layout of final system FOV.

3.5. Optical Instrument Indices

The overall indices of the optical design are shown in Table 5.

Table 5. Summary of optical indices.

Parameter	Value
Wavelength coverage	Spectral: 2–8 µm; pointing: 0.5–2 µm
F number	14.754 (2–4 µm); 7.377 (4–8 µm)
Resolving power	∼100 (2–4 µm); ∼30 (4–8 µm)
SNR	∼7
Entrance aperture	≥1.5 m
System throughput	≥0.4
FOV	Diffraction limited: 27.9″; unvigneting: 44″

4. Results of Optical-System Design and Simulation

In order to detect the spectrum of an exoplanetary atmosphere, an optimized optical system is essential. According to the above astronomical parameters and optical-system indices, a feasible instrumentation proposal was designed, and performance is evaluated in this section.

The researchers conducted simulation experiments [38] to determine the appropriate operating temperature. The major effect in the temperature variation of the detector is that of a changing dark current. Peak-to-peak variation in the temperature of optical elements results in the modulation of its thermal emission. When the operating temperature of the optical elements is set to ≤70 K, and that of detectors to ≤40 K, the thermal-radiation noise caused by elements and the detector noise could be limited. Devices performance and refractive lens indices should be considered in optical-system design at such temperatures.

The overall optical system consists of four modules: telescope, dichroic system, pointing system, and infrared spectrometer. The telescope is used to collect spectral radiation from stars. The dichroic system splits light and delivers beams to modules. The pointing system is utilized for photometry and orientation. The infrared spectrometer is the main scientific payload to provide dispersive spectra with a specific spectral resolution and SNR in the detection waveband.

4.1. Telescope

The telescope design has an off-axis dual-paraboloid mirror structure, of which the primary and secondary mirrors are eccentric along the *Y* axis. It has the advantage of higher optical efficiency due to having fewer components compared with a traditional Cassegrain telescope, and it is suitable for small FOV systems because the parabolic mirror can perfectly image the on-axis point, but cannot meet the aplanatic condition.

The primary and secondary mirrors are both circular aperture mirrors. There is a focus point between the two mirrors that can be used to limit stray light. The telescope collects parallel beams from distant astronomical targets by the 2.1 m diameter primary mirror, and the beams are then compressed as collimated beams with smaller apertures and injected into the dichroic system. The detailed optical design parameters of the telescope are listed in Table 6.

Table 6. Optical-design parameters of telescope.

Parameter	Value
Wavelength coverage	0.5–8 μm
FOV	Diffraction limited: 27.9″, unvignetted: 44″
Collecting area	3.46 m^2
Aperture	2.1 m
Output-beam dimension	0.2 m
Angular magnification	−10.5

The telescope's optical system meets the performance requirements. The spot diagram (Figure 5a) on the image surface of the telescope system shows that the spot radius at a wavelength of 4 μm in 7 characteristic sampling fields (as shown in the 7 boxes in the figure) is close to zero, far less than the Airy radius of 0.02905 mrad. The spot diagram indicates that the radius of the geometric encircling circle of the image point is much smaller than that of the Airy spot at the central wavelength, which means that the telescope can realize diffraction limit imaging. Figure 5b is a field map of the root-mean-square (RMS) wavefront error (WFE) at the imaging surface, which is used to show WFE distribution according to the FOV. As shown in Figure 5b, the RMS WFE at 4 μm wavelength was less than 7.6 nm (0.0019 λ) in full FOV, far less than the diffraction limit of 288 nm (0.072 λ).

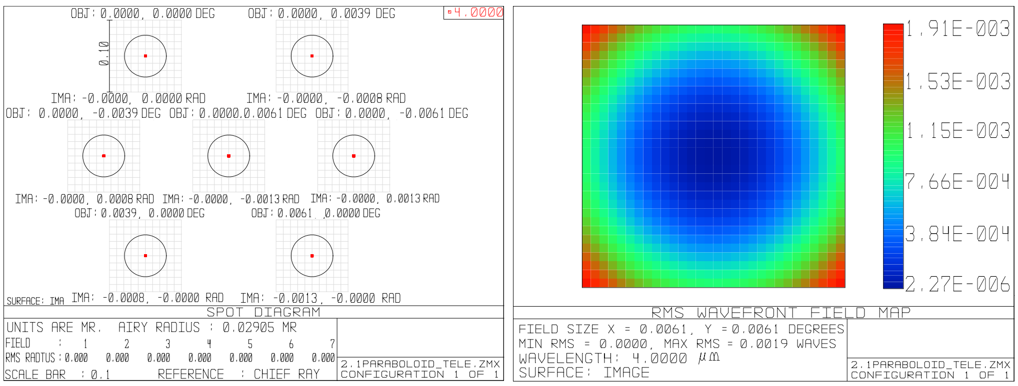

(**a**) (**b**)

Figure 5. (**a**) Spot diagram at different FOVs of telescope output. Red spots, image spots; black circles, Airy spots. FOV and parallelism of output beams shown above and below each box, respectively. Imaging spots in the required FOV were far smaller than Airy spots. (**b**) RMS WFE map over full FOV at telescope output.

4.2. Dichroic System

The light from the telescope is divided into three channels by two dichroic beam-splitters in the dichroic system. The beam-splitting plane is perpendicular to the Y axis. A collimated beam in 0.5–2 μm is delivered into the pointing system, focused beams over 2–4 μm (CH1) and 4–8 μm (CH2) are injected into two entrance slits of the spectrometer channels by parabolic focus mirrors.

According to the above principle, ZEMAX optical software was used to plot the layout of the dichroic system, as shown in Figure 6a, in which blue, green, and red represent the channels of the pointing system, CH1, and CH2, respectively. Figure 6b shows the shaded model of the dichroic system combined with the telescope.

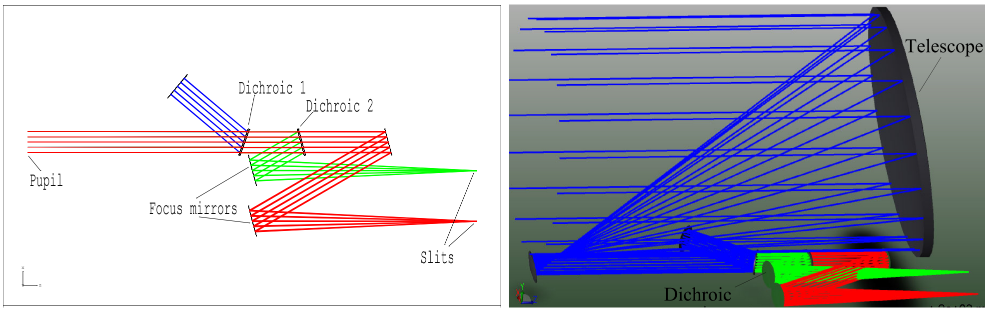

(**a**) (**b**)

Figure 6. (**a**) Dichroic system. (**b**) Shaded model of dichroic system combined with telescope. CH1 channel, green; CH2, red; pointing system, blue.

Figure 7 shows the field maps of RMS WFEs at the exit of dichroic system for (a) CH1 and (b) CH2. Similar to Figure 5b, Figure 7 evaluates the imaging performance of light passing through the dichroic system and telescope. Maximal RMS WFEs at the maximal wavelength of CH1 and CH2 were 0.2544 µm (0.0636 λ) and 0.2568 µm (0.0321 λ), which were less than the diffraction limit of 0.072 λ. Figure 8 shows the matrix-spot diagrams at the exit of the dichroic system (slit surface) for CH1 and CH2. The radii of the image points in each FOV were smaller than the Airy radius.

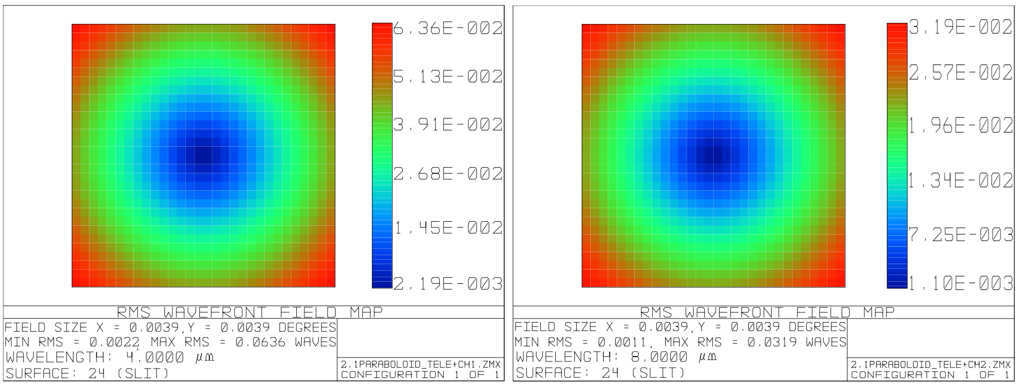

(**a**) (**b**)

Figure 7. Root-mean-square (RMS) wavefront error (WFE) maps over full FOV at exit of dichroic system for (**a**) CH1 and (**b**) CH2.

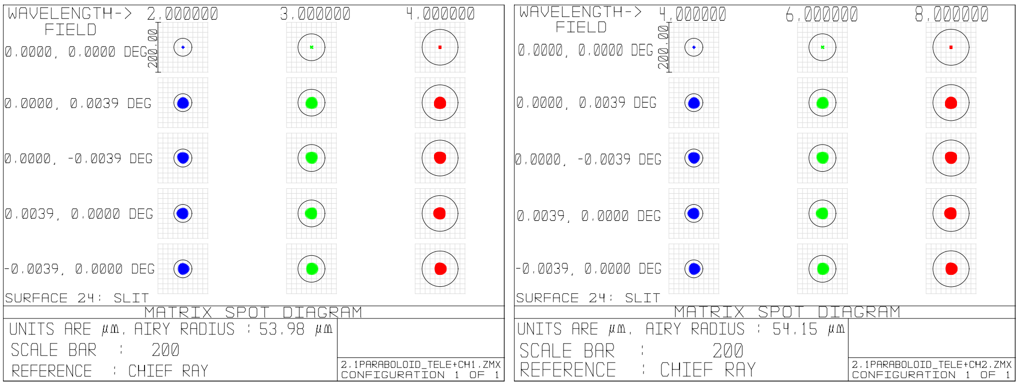

(**a**) (**b**)

Figure 8. Matrix spot diagrams at exit of dichroic system (slit surface) for (**a**) CH1 and (**b**) CH2. Different boxes show image spots and Airy spots at different FOVs and wavelengths. (**a**) Spot diagram of CH1. Boxes in different rows correspond to different FOVs. Second, third, and fourth columns show imaging results at the exit of dichroic system at wavelengths of 2, 3, and 4 µm, respectively.

4.3. Infrared Spectrometer

Due to the particularity of observed targets, the design requirements of infrared spectrometer have the characteristics of lower spectral resolution demand, higher system stability and throughput, no angular resolution. Therefore, a prism-dispersing spectrometer is selected as the design proposal, which has higher optical efficiency at required resolution than that of others, increasing the photoelectron count in spectral resolution elements and decreasing influence of the dark current and readout noise to signal. Additionally, prism can reduce the stray light caused by manufacture tolerance as well.

The spectrometer module is connected to the dichroic system. The focused beam from dichroic enters two independent channels (CH1 and CH2) of the infrared spectrometer through slit. Then it is shaped into parallel beam by collimator and dispersed to spectrum by prisms. Finally, the spectrum is focused on the detector by lenses of camera. Compared with the double lens scheme, the off-axis parabolic mirror scheme is adopted as the collimator to improve the throughput and reduce the influence of chromatic aberration. The optical parameters of infrared spectrometer are summarized in Table 7. The layouts of two spectrometer channels are shown in Figure 9.

Table 7. Summary of optical parameters of infrared spectrometer.

Parameters	CH1 (2–4 µm)	CH2 (4–8 µm)
Input F/#	f/10.8	f/10.8
Slit size	0.33 mm × 2.2 mm	0.43 mm × 2.2 mm
Prism material	CaF_2	CaF_2
Prism apex and incidence angle	29.4° and 39.6°	8.9° and 9.1°
Camera material	Silicon and germanium	CaF_2 and ZnS
Airy radius in λ_{min}	36 µm	36 µm
PSF sampling λ_{min} and λ_{max}	2 and 4 pix	2 and 4 pix
Pixel scale	0.12″/pixel	0.24″/pixel
Pixel size	18 µm	18 µm

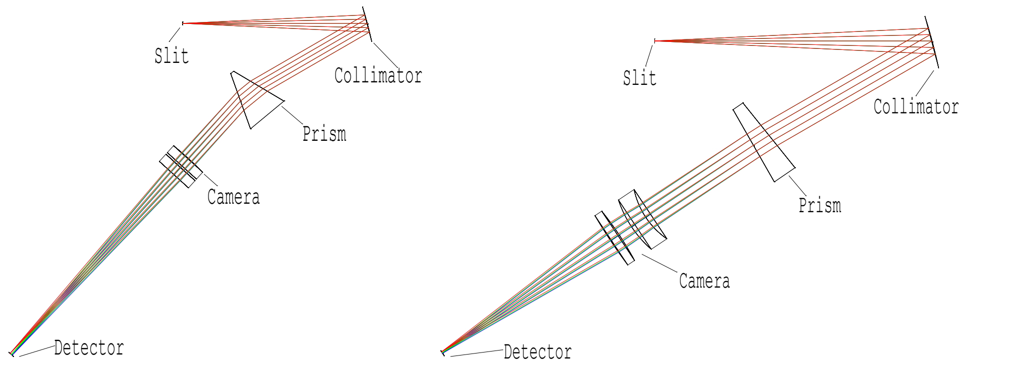

Figure 9. Layouts of (**a**) CH1 and (**b**) CH2. Two independent channels (CH1 and CH2) are connected to dichroic-system slits. The focused beams from the slits are shaped into parallel beams by collimators and dispersed to spectra by prisms. Lastly, spectra are focused on detectors by lenses of cameras. CH1 and CH2 cover different wavelengths with varying spectral resolutions.

The overall design of optical system is shown in Figure 10, including the telescope, dichroic system, and spectrometer.

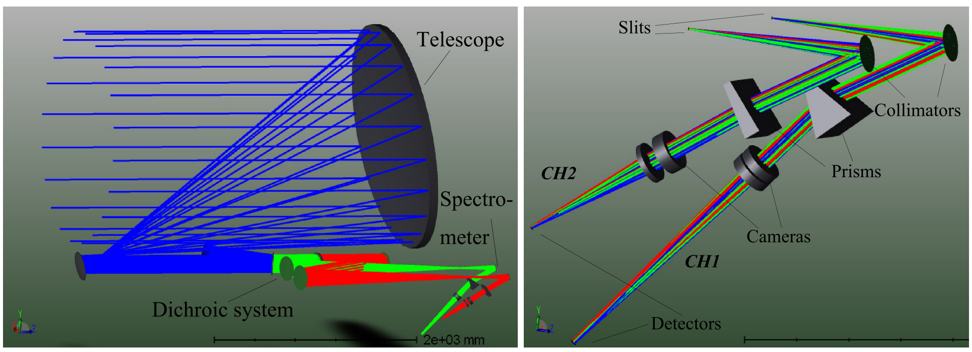

Figure 10. (**a**) Overall structure of optical system, including telescope, dichroic system, and spectrometers. FGS, CH1, and CH2 channels represented by blue, green, and red, respetively. (**b**) Spectrometer details in the optical system. Different light colors distinguish wavelengths in each channel.

Combined with the proposed optical system, the optical performance of the spectrometer is evaluated. Spot diagrams and PSF curves of two channels at the maximal and minimal wavelengths are shown in Figure 11. For example, in (a) left, there are 5 boxes in the spot diagram that correspond to imaging spots at different FOVs. Blue and green spots represent imaging spots with wavelengths of 2 and 2.018 μm, respectively. Black circles denote Airy rings. The image spots of each wavelength were diffraction-limited in the required FOV; (a) right shows the PSF curve distributed along the Y axis in the central FOV. Two peaks of the curve correspond to image spots with wavelengths of 2 and 2.018 μm. At the minimal wavelength of CH1, spots could be distinguished when $\Delta\lambda$ = 0.018 μm. Moreover, the resolution for CH1 was estimated to be 111–200, and for CH2 is 43–94. Figure 12 shows the PSF curve distributed along the Y axis at minimal wavelength (λ_{min}) in each channel.The first dark rings of PSF were located at 36 μm for both CH1 and CH2, which means that the FWHM at all wavelengths was no less than 36 μm. Thus, at least 2-pixel FWHM sampling can be provided when the detector pixel size is 18 μm.

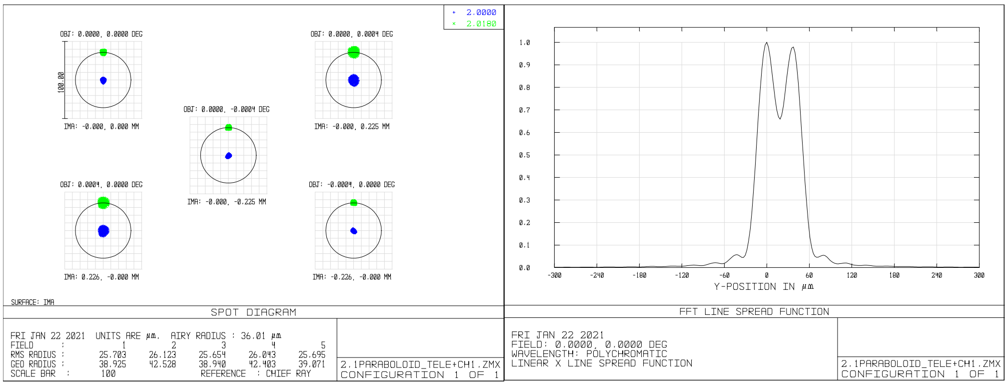

(**a**)

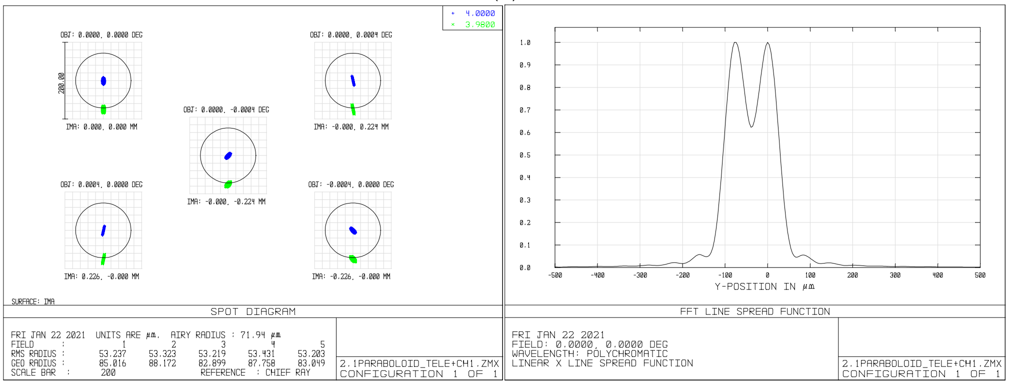

(**b**)

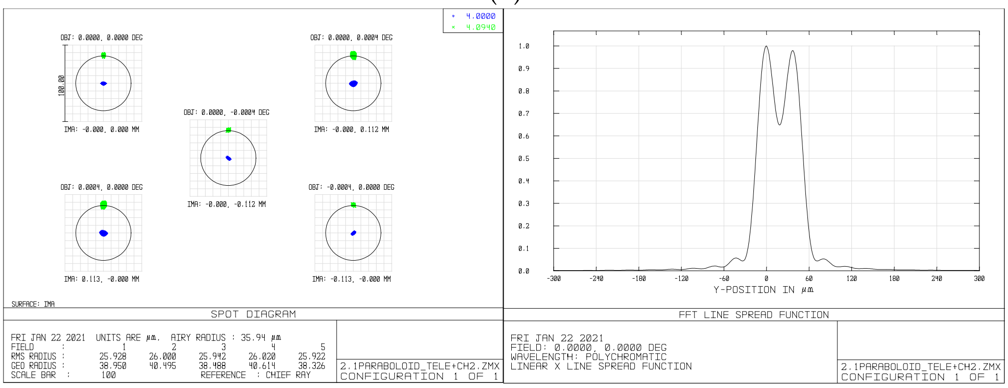

(**c**)

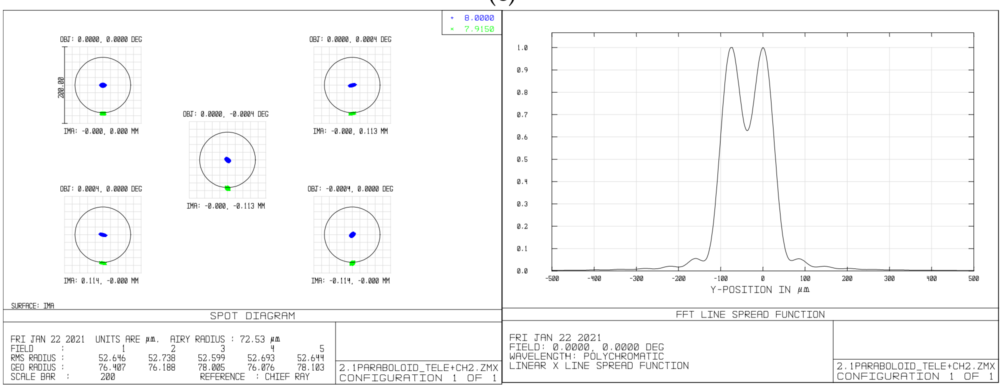

(**d**)

Figure 11. Spot diagrams and PSF curves of different channels and wavelengths (**a**) for CH1 at minimal wavelength, (**b**) for CH1 at maximal wavelength, (**c**) for CH2 at minimal wavelength, and (**d**) for CH2 at maximal wavelength.

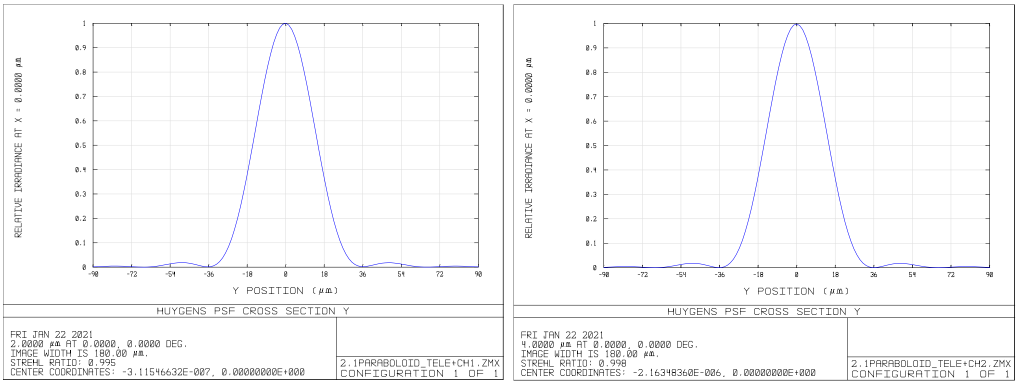

(**a**) (**b**)

Figure 12. PSF curves for (**a**) CH1 and (**b**) CH2 in λ_{min}. Optical system of two channels was designed to achieve 2-pixel full width at half-maximum (FWHM) sampling when pixel size is 18 µm.

5. Conclusions

To study the characteristics of an exoplanetary atmosphere, a novel optical system based on transit spectroscopy was designed. The optical-system indices were systematically analyzed on the basis of the principles of astronomy and optics, of which the transit SNR was introduced into the determination of telescope aperture and throughput. Furthermore, a modular design of optical system within index requirements is newly presented.

In order to detect transit spectrum, the parameter requirements of optical system are derived. Wavelength coverage is selected via the target characteristic, and the F number is determined according to the relationship between PSF and pixel size under given wavelength distribution. Spectral resolution and SNR are limited according to existing retrieval codes. Telescope aperture and overall throughput were discussed according to the potential for the realization of the goal SNR during missions. Combined with pointing accuracy, Airy spot, and assembly tolerance, telescope and payload FOV assignments are listed. The operating environment of the instrument, including temperature and orbit, was also considered. Optical indices of instrument are listed.

Furthermore, a feasible optical system was proposed, and performance was evaluated to verify the validity of the indices. The simulation showed that the design and performance met the requirements. The off-axis dual-paraboloid mirror telescope, designed with a 2.1 m aperture to reach the goal SNR, was matched with a dichroic system to provide diffraction-limited input beams for payloads. The spectral resolutions of the dual-channel spectrometer were 111–200 and 43–94. The image points in each wavelength were smaller than the Airy spot within slit FOV, and the PSF FWHM at λ_{min} was 36 µm providing 2 pixels of 18 µm sampling. The overall optical system achieved good performance and met the index requirements, which could achieve the scientific goal of studying the atmospheric characteristics of exoplanets.

In order to obtain a larger collection area and sufficient SNR, a primary mirror of the telescope with a larger aperture was designed in this simulation study. However, larger-aperture mirrors have higher requirements for the carrying capacity of aircraft, and the corresponding manufacturing technology of mirrors still needs to be improved. Therefore, in a future study, methods to improve SNR should be deeply discussed to reduce the requirements of telescope apertures, and the improvement of mirror-manufacturing technology should be paid more attention.

Author Contributions: Conceptualization, F.W.; methodology, F.W.; software, X.D.; validation, Y.P.; formal analysis, X.F.; investigation, F.W.; resources, H.W.; data curation, X.L.; writing—original-draft preparation, F.W.; writing—review and editing, Y.S.; visualization, X.D.; supervision, H.W.; project administration, X.F.; funding acquisition, S.L. All authors have read and agreed to the published version of the manuscript.

Funding: This research was funded by National Natural Science Foundation of China (NSFC) grant number 11803075.

Institutional Review Board Statement: Not applicable.

Informed Consent Statement: Not applicable.

Data Availability Statement: Data are contained within the article.

Conflicts of Interest: The authors declare no conflict of interest.

References

1. Kaltenegger, L.; Lin, Z. Finding Signs of Life in Transits: High-resolution Transmission Spectra of Earth-line Planets around FGKM Host Stars. *Astrophys. J. Lett.* **2021**, *909*, L2. [CrossRef]
2. Morello, G.; Zingales, T.; Martin-Lagarde, M.; Gastaud, R.; Lagage, P.O. Phase-curve Pollution of Exoplanet Transmission Spectra. *Astron. J.* **2021**, *161*, 174. [CrossRef]
3. Zhang, X. Atmospheric regimes and trends on exoplanets and brown dwarfs. *Res. Astron. Astrophys.* **2020**, *20*, 99. [CrossRef]
4. Wang, F.; Fan, X.; Wang, H.; Shen, Y.; Pan, Y. Exoplanet detection methods and transit spectrometer equipment of astronomical telescopes. In Proceedings of the AOPC 2020: Optical Sensing and Imaging Technology, Beijing, China, 30 November–2 December 2020; Volume 11567, p. 558.
5. Beichman, C.; Benneke, B.; Knutson, H.; Smith, R.; Lagage, P.O.; Dressing, C.; Latham, D.; Lunine, J.; Birkmann, S.; Ferruit, P.; et al. Observations of transiting exoplanets with the James Webb Space Telescope (JWST). *Publ. Astron. Soc. Pac.* **2014**, *126*, 1134–1173. [CrossRef]
6. Line, M.R.; Stevenson, K.B.; Bean, J.; Desert, J.M.; Fortney, J.J.; Kreidberg, L.; Madhusudhan, N.; Showman, A.P.; Diamond-Lowe, H. No thermal inversion and a solar water abundance for the hot Jupiter HD 209458b from HST/WFC3 spectroscop. *Astron. J.* **2016**, *152*, 203. [CrossRef]
7. Encrenaz, T.; Tinetti, G.; Coustenis, A. Transit spectroscopy of temperate Jupiters with ARIEL: A feasibility study. *Exp. Astron.* **2018**, *46*, 31–44. [CrossRef]
8. Tinetti, G.; Vidal-Madjar, A.; Liang, M.C.; Beaulieu, J.P.; Yung, Y.; Carey, S.; Barber, R.J.; Tennyson, J.; Ribas, I.; Allard, N.; et al. Water vapour in the atmosphere of a transiting extrasolar planet. *Nature* **2007**, *448*, 169–171. [CrossRef] [PubMed]
9. Seager, S.; Sasselov, D.D. Theoretical transmission spectra during extrasolar giant planet transits. *Astrophys. J.* **2000**, *537*, 916–921. [CrossRef]
10. Deming, D. Quest for a habitable world. *Nature* **2008**, *456*, 714–715. [CrossRef] [PubMed]
11. Mugnai, L.V.; Pascale, E.; Edwards, B.; Papageorgiou, A.; Sarkar, S. ArielRad: The Ariel radiometric model. *Exp. Astron.* **2020**, *50*, 303–328. [CrossRef]
12. Brown, T.M. Transmission Spectra as Diagnostics of Extrasolar Giant Planet Atmospheres. *Astrophys. J.* **2001**, *553*, 1006–1026. [CrossRef]
13. Louie, D.R.; Deming, D.; Albert, L.; Bouma, L.G.; Bean, J.; Lopez-Morales, M. Simulated JWST /NIRISS Transit Spectroscopy of Anticipated Tess Planets Compared to Select Discoveries from Space-based and Ground-based Surveys. *Publ. Astron. Soc. Pac.* **2018**, *130*, 044401. [CrossRef]
14. Berta, Z.K.; Charbonneau, D.; Désert, J.M.; Miller-Ricci Kempton, E.; McCullough, P.R.; Burke, C.J.; Fortney, J.J.; Irwin, J.; Nutzman, P.; Homeier, D. The flat transmission spectrum of the super-earth GJ1214b from Wide Field Camera 3 on the Hubble Space Telescope. *Astrophys. J.* **2012**, *747*, 35. [CrossRef]
15. Sarkar, S. Exoplanet Transit Spectroscopy: Development and Application of a Generic Time Domain Simulator. Ph.D. Thesis, Cardiff University, Cardiff, UK, 2017.
16. Rauer, H.; Gebauer, S.; Paris, P.V.; Cabrera, J.; Godolt, M.; Grenfell, J.L.; Belu, A.; Selsis, F.; Hedelt, P.; Schreier, F. Potential biosignatures in super-Earth atmospheres. *Astron. Astrophys.* **2011**, *529*, A8. [CrossRef]
17. Seager, S.; Mallen-Ornelas, G. A Unique Solution of Planet and Star Parameters from an Extrasolar Planet Transit Light Curve. *Astrophys. J.* **2003**, *585*, 1038–1055. [CrossRef]
18. Tinetti, G. The ARIEL Mission Proposal—A Candidate for the ESA M4 Mission. 2015. Available online: http://ariel-spacemission.eu/yellow-book-technical-documents (accessed on 30 March 2021).
19. Encrenaz, T.; Tinetti, G.; Tessenyi, M.; Drossart, P.; Hartogh, P.; Coustenis, A. Transit spectroscopy of exoplanets from space: How to optimize the wavelength coverage and spectral resolving power. *Exp. Astron.* **2015**, *40*, 523–543. [CrossRef]
20. Leinert, C.; Bowyer, S.; Haikala, L.K.; Hanner, M.S.; Hauser, M.G.; Levasseur-Regourd, A.C.; Mann, I.; Mattila, K.; Reach, W.T.; Schlosser, W.; et al. The 1997 reference of diffuse night sky brightness. *Astron. Astrophys. Suppl. Ser.* **1998**, *127*, 1–99. [CrossRef]
21. Tinetti, G.; Drossart, P.; Eccleston, P. A chemical survey of exoplanets with ARIEL. *Exp. Astron.* **2018**, *46*, 135–209. [CrossRef]
22. Barstow, M.A.; Barstow, J.K.; Casewell, S.L.; Holberg, J.B.; Hubeny, I. Evidence for an external origin of heavy elements in hot DA white dwarfs. *Mon. Not. R. Astron. Soc.* **2014**, *440*, 1607–1625. [CrossRef]
23. Tinetti, G.; Encrenaz, T.; Coustenis, A. Spectroscopy of planetary atmospheres in our Galaxy. *Astron. Astrophys. Rev.* **2013**, *21*, 63. [CrossRef]

24. Al-Refaie, A.F.; Changeat, Q.; Waldmann, I.P.; Tinetti, G. TauREx III: A fast, dynamic and extendable framework for retrievals. *arXiv* **2019**, arXiv:1912.07759.
25. Waldmann, I.P.; Rocchetto, M.; Tinetti, G.; Barton, E.J.; Yurchenko, S.N.; Tennyson, J. Tau-REx II: Retrieval of emission spectra. *Astrophys. J.* **2015**, *813*, 13. [CrossRef]
26. Pan, Y.; Wang, H.; Jing, N.; Shen, Y.; Xue, Y.K.; Liu, J. Parameter selection and optical design of all-day star sensor. *Acta Photonica Sin.* **2016**, *45*, 0122002. [CrossRef]
27. Sarkar, S.; Papageorgiou, A.; Pascale, E. Exploring the potential of the ExoSim simulator for transit spectroscopy noise estimation. In Proceedings of the Space Telescopes and Instrumentation 2016: Optical, Infrared, and Millimeter Wave, Edinburgh, UK, 26 June–1 July 2016; Volume 9904, p. 99043R.
28. Pascale, E.; Waldmann, I.P.; MacTavish, C.J.; Papageorgiou, A.; Amaral-Rogers, A.; Varley, R.; de Foresto, V.C.; Griffin, M.J.; Ollivier, M.; Sarkar, S.; et al. EChOSim: The Exoplanet Characterisation Observatory software simulator. *Exp. Astron.* **2014**, *40*, 601–619. [CrossRef]
29. Sarkar, S.; Madhusudhan, N.; Papageorgiou, A. JexoSim: A time-domain simulator of exoplanet transit spectroscopy with JWST. *Mon. Not. R. Astron. Soc.* **2020**, *491*, 378–397. [CrossRef]
30. Sarkar, S.; Pascale, E. ExoSim: A novel simulator of exoplanet spectroscopic observations. *Eur. Planet. Sci. Congr.* **2015**, *10*, EPSC2015-187.
31. Rein, H. A proposal for community driven and decentralized astronomical databases and the Open Exoplanet Catalogue. *arXiv* **2012**, arXiv:1211.7121.
32. Allard, F.; Homeier, D.; Freytag, B. Models of very-low-mass stars, brown dwarfs and exoplanets. *Philos. Trans. R. Soc. A Math. Phys. Eng. Sci.* **2012**, *370*, 2765–2777. [CrossRef]
33. Mandel, K.; Agol, E. Analytic light curves for Planetary Transit Searches. *Astrophys. J.* **2002**, *580*, L171–L175. [CrossRef]
34. McMurtry, C.; Lee, D.; Beletic, J.; Chen, C.Y.A.; Demers, R.T.; Dorn, M.; Edwall, D.; Fazar, C.B.; Forrest, W.J.; Liu, F.; et al. Development of sensitive long-wave infrared detector arrays for passively cooled space missions. *Opt. Eng.* **2013**, *52*, 091804. [CrossRef]
35. Da Deppo, V.; Pace, E.; Morgante, G.; Focardi, M.; Terraneo, M.; Zocchi, F.E.; Bianucci, G.; Micela, G. A prototype for the primary mirror of the ESA ARIEL mission: Design and development of an off-axis 1-m diameter aluminium mirror for infrared space applications. In Proceedings of the Advances in Optical and Mechanical Technologies for Telescopes and Instrumentation III, Austin, TX, USA, 10–15 June 2018; Volume 1070632, p. 110.
36. Da Deppo, V.; Middleton, K.; Focardi, M.; Morgante, G.; Pace, E.; Claudi, R.; Micela, G. Design of an afocal telescope for the ARIEL mission. In Proceedings of the Space Telescopes and Instrumentation 2016: Optical, Infrared, and Millimeter Wave, Edinburgh, UK, 26 June–1 July 2016; Volume 9904, p. 990434.
37. Eccleston, P. *ARIEL Payload Design Description*; ARIEL-RAL-PL-DD-001; ARIEL Payload Consortium: Paris, France, 2017. Available online: https://arielspacemission.files.wordpress.com/2017/05/sci-2017-2-ariel.pdf (accessed on 30 March 2021).
38. Morgante, G.; Terenzi, L.; D'Ascanio, D.; Eccleston, P.; Crook, M.; Hunt, T.; Da Deppo, V.; Focardi, M.; Micela, G.; Malaguti, G.; et al. Thermal architecture of the ESA ARIEL payload. In Proceedings of the Space Telescopes and Instrumentation 2018: Optical, Infrared, and Millimeter Wave, Austin, TX, USA, 10–15 June 2018; Volume 10698, p. 154.